Hybrid microwave sintering of Zirconia Toughened Alumina in a multimode cavity – Influence of the content of 3 mol% yttria stabilized zirconia and sintering configurations

Nouhaila Khalile, Clémence Petit, Christophe Meunier, François Valdivieso

Hybrid microwave sintering of Zirconia Toughened Alumina in a multimode cavity – Influence of the content of 3 mol% yttria stabilized zirconia and sintering configurations

Nouhaila Khalile, Clémence Petit*, Christophe Meunier, François Valdivieso

Mines Saint-Etienne, Univ Lyon, CNRS, UMR 5307 LGF, Centre SMS, F-42023 Saint-Etienne France

*Corresponding author:

Clémence Petit

Clemence.petit@emse.fr

Mines Saint-Etienne, Univ Lyon, CNRS, UMR 5307 LGF, Centre SMS, F-42023 Saint-Etienne France

Abstract

MW sintering is a sintering process in which samples directly heat by absorption of the electromagnetic field, leading to a fast volume heating. Thus, the materials are heated due to their own dielectric properties. Zirconia Toughened Alumina (ZTA) is of particular interest for MW sintering because of the difference of dielectric properties between alumina and zirconia. In this study, ZTA pellets with different volume fractions of zirconia were sintered in a MW multimode cavity with different sintering cells, *i.e.*, with or without susceptor. These experiments show that all the samples were densified whatever the configuration. But the evolution of power and temperature vs time during the sintering cycle shows a better heating capability when the volume fraction of zirconia increases. The influence of the material to heat is more visible when sintering without susceptor. This was confirmed by other experiments, where the samples were heated by a constant incident power in a single-mode cavity.

Keywords: Zirconia Toughened Alumina, Microwave sintering, Dielectric properties

1. Introduction

Alumina and zirconia are the most famous inert bioceramics, especially used in orthopaedic and dental applications [1, 2, 3]. Alumina combines biocompatibility, high hardness and high Young's modulus. But its low fracture toughness has prevented its use, especially in the dental field [4]. Zirconia is also biocompatible and exhibits excellent mechanical properties, especially a high fracture toughness, which is related to the so-called transformation toughening mechanism. Zirconia exists naturally in three allotropic crystalline structures: monoclinic (m, from room temperature up to 1170 °C), tetragonal (t, from 1170°C to 2370 °C) and cubic (c, from 2370°C to melting point, 2710°C) [5]. The transformation from the t to the m phase during cooling is accompanied to an increase of volume (around 4%) which is responsible of failure. The t phase can be stabilized at room temperature by doping zirconia with cations like yttrium [6]. The transformation-toughening mechanism consists in the ability of the metastable tetragonal grains to undergo a stress-mediated phase transformation to the monoclinic phase. This phenomenon is responsible for the high fracture toughness of yttria-stabilized tetragonal zirconia polycrystals (Y-TZP) [7]. The only limit of 3Y-TZP materials is aging phenomenon, also known as Low Temperature Degradation (LTD). In the presence of water, the t-m transformation occurs from the surface and leads to micro-cracking and roughening [8]. Zirconia-toughened alumina (ZTA) has been proposed as a solution to overcome the main disadvantages of each monolithic material. In this ceramic-ceramic composite, zirconia grains are dispersed in the alumina matrix. ZTA is known to exhibit high toughness, hardness and good resistance to LTD [9-11].

The final properties of bioceramics are particularly related to their microstructures. The precise control of all steps of fabrication processes (*i.e.*, synthesis of powder, shaping and sintering) are required to obtain final products with high densities and fine microstructures. In the last decades, the ceramist community has focused efforts towards so-called advanced fabrication

processes (mainly shaping by additive manufacturing [12, 13] and rapid sintering processes [14, 15, 16]) as greener alternatives to traditional processes. Additive manufacturing is an alternative approach to conventional shaping processes (as pressing or colloidal processes) which makes possible the manufacturing of geometrically complex near-net-shape parts without expensive tooling. Rapid sintering processes, such as microwave (MW) sintering [14], Spark Plasma Sintering [15] or cold sintering [16] enable to densify ceramics with higher heating rates or lower temperatures, in comparison with conventional (CV) sintering in a classical resistive furnace. These advanced processes are of particular interest for bioceramics where patient-specific components (single parts or small production volume) with a rapid production are often required [17].

MW sintering is a rapid sintering process and presents the advantage of being a pressureless process (contrary to SPS or cold sintering) [18, 19]. In MW sintering, the material interacts directly with the electromagnetic field, causing a volumetric heating of the samples [20]. Consequently, it leads to much higher heating rates and to a uniform temperature distribution within the solid. Under MW field, a material heats by its own dielectric properties. Two main dielectric properties are responsible of coupling capability of materials: the complex permittivity (ε^*) and the loss tangent (tan α). ε^* can be defined by the following formula: $\varepsilon^* = \varepsilon' - j\varepsilon''$ where ε' is dielectric constant, ε'' is dielectric loss factor, and $tan(\alpha) = \varepsilon''/\varepsilon'$. The higher dielectric loss factor, the more material couples with the electromagnetic field and heats up quickly. Therefore, understanding the MW/material interactions is very important to optimize MW sintering and to obtain fully dense sample with fine-grained microstructures.

Different studies have been performed about MW sintering of ZTA [21-23]. These authors often highlight the possibility to obtain highly dense materials with fine grain sizes with lower temperature and lower duration, in comparison with CV sintering. However, up to now, few researches have been conducted to understand the MW/materials interactions for ZTA. This

topic is particularly interesting for ZTA because of the presence of two materials with different dielectric properties. Alumina is a low-loss dielectric material and it is considered as transparent to MW radiation [24]. That is why it is always sintered using an external susceptor. A susceptor is a material which strongly couples with MW and can transmit heat to the sample, mainly by radiation [25]. In the case where a susceptor is used, MW heating is called hybrid or indirect. Silicon carbide (SiC) is often used as a susceptor to sinter low-loss materials like alumina [26]. 3Y-TZP couples better with MW than alumina. Its loss tangent sharply increases with temperature [27]. This behaviour can create difficulties to control its heating rate under MW, and thus to control the sintering cycle [27, 28]. Due to this behaviour, 3Y-TZP has already been used as a susceptor in MW sintering. For example, Heuguet *et al.* studied MW hybrid sintering of alumina with 3Y-TZP or SiC susceptor [29]. They demonstrated that a 3Y-TZP susceptor favours a direct MW/alumina interaction whereas a SiC susceptor leads to a dominating indirect heating. It was attributed to the high loss tangent and low electrical conductivity of 3Y-TZP at high temperatures. It can be hypothesized that 3Y-TZP can play the role of an "internal susceptor" during MW sintering of ZTA. Varying the ZrO_2 content in the ZTA samples can lead to various behaviours under MW.

This work is focused on the study of MW sintering of different ZTA samples. Two different 3Y-TZP volume fractions were considered. To study a possible susceptor effect of zirconia, the samples were sintered in a multimode MW cavity in two configurations, *i.e.*, with or without the use of a SiC susceptor. Monolithic alumina and 3Y-TZP samples were also sintered, as reference materials. The results for MW-sintered samples were compared to the ones of CV sintering. To complete these experiments, the same samples were also heated in a MW single-mode resonant cavity.

2. Experimental procedures

2.1. Preparation of samples

High purity commercial alumina (purity > 99.9%, *BMA-15, Baikowski International*) and 3Y-TZP (purity > 99.8%, *TOSOH Corporation*) powders were used as starting materials. ZTA powders with different amounts of zirconia were prepared. Two compositions were manufactured: 80 vol% alumina/20 vol% 3Y-TZP and 90 vol% alumina/10 vol% 3Y-TZP. For each composition, a suspension with a solid loading of 60 vol% was prepared by adding adequate amounts of alumina and zirconia powders in distilled water. The suspension was dispersed by addition of 2.7 wt% of Darvan CN dipersant (*Vanderbilt minerals, LLC*). The amount was chosen according to preliminary tests (not shown here). The pH of the suspension was adjusted to 10 by addition of KOH. After addition of 2 wt% of PVA binder (*Rhodoviol 4/125, Prolabo*) and 1 wt% polyethylene glycol (*Mw 1500, Prolabo*), the suspension was ball-milled during 15 hours using 2 mm-diameter alumina balls. Finally the suspension was spray-dried with a spray-dryer (*mini spray-dryer BUCHI 190*).

The resulting powders were shaped into disks by uniaxial pressing (12 mm diameter with 4 mm thickness for MW sintering and 8 mm diameter with 8 mm thickness for CV sintering) at 50 MPa and then isostatically pressed at 300 MPa. The dimensions of the pellets were adjusted to the experimental devices (*i.e.*, sintering cell in the MW cavity and sample holder in the dilatometer). Alumina and 3Y-TZP pellets were also prepared for comparison purposes.

The samples were debinded by heating at 1°C/min to 600°C with a dwell of 1 hour in air. All the green samples had a relative density of 50-52 %, relative to theoretical density (T.D.).

MW sintering was carried out in the multimode cavity described in the subsection 2.2. The samples were sintered inside the insulation box described in the subsection 2.3 in two configurations: with and without the susceptor (noted MW-SiC and MW-noSiC respectively).

Different pellets were also conventionally sintered in air in a dilatometer (*Setsys 16/18, SETARAM*).

The same thermal cycle was applied for CV and MW sintering experiments: heating rate of 25°C/min to 1550°C and a dwell time of 10 min. The aim was to compare the densification curves.

The samples will be named hereafter: A for alumina pellets, 3YZ for 3Y-TZP pellets and A-10-3YZ and A-20-3YZ for the two types of ZTA pellets.

2.2. The multimode MW cavity

MW sintering experiments were performed in a MW heating system already described in previous papers [30, 31]. This heating device was equipped with a fixed frequency of 2.45 GHz~3kW MW generator (*GMP30K, SAIREM*) connected to a multimode cavity of dimension of 430 mm × 430 mm × 490 mm.

One of the main difficulties with the MW heating is the temperature measurement. Thus, in order to avoid disturbance of the electromagnetic waves in the cavity, contactless measurement of temperature using infrared pyrometers was performed. A bichromatic pyrometer (*Lumasense Technology*) sensitive to the wavelength between 2 and 2.5 µm, working in the 250-1800 °C temperature range was used. The pyrometer measures the spectral radiance of the surface of the sample from a spot diameter of approximately 5 mm. To obtain an accurate value of temperature, it is necessary to know the ratio of apparent emissivity *k* in the experimental conditions. Therefore, a calibration method based on the melting point of a metallic calibration material as described by Zymełka *et al.* [32] was used. In this study, palladium (Pd: $T_{melting}$ = 1550 °C) was used as calibrating material. It was placed on a small hole engraved in the sample surface. When Pd starts melting, the ratio *k* of the IR pyrometer is recalculated so that the melting point of Pd is equal to the measured temperature. After three series of measurements,

the average values of the ratio of apparent emissivity *k* are 1.01, 0.9547 and 0.991 for Al_2O_3, 3YZ and A-20-3YZ respectively.

Optical dilatometry was used to record the pellet's shrinkage during sintering. The protocol used in this work was previously described by Zuo *et al.* [33] and Meunier *et al.* [34]. A high-resolution CCD camera (*SLC2050MTLGEC; 14-bit, 1600 9 1200, SVS-VISTEK)* records pictures of the flat circular surface of the pellet during the thermal cycle. Then, the recorded images were recorded by a dedicated custom made Labview software which detects the pellets' edges to measure the diameter. The program finally outputs the evolution of the pellet's diameter during sintering. However, in CV dilatometry, the sample's height is recorded. In order to compare the dilatometric data of CV and MW sintering, the evolution of relative density was calculated with the Eq. 1 (for CV dilatometry) and Eq. 2 (for MW dilatometry), taking into account the anisotropy shrinkage ratio α (Eq. 3).

$$\rho(t) = \frac{\left(1+\frac{h_f-h_0}{h_0}\right)*\left(1+\frac{D_f-D_0}{D_0}\right)^2}{\left(1+\frac{h(t)-h_0}{h_0}\right)*\left(1+\alpha\frac{h(t)-h_0}{h_0}\right)^2} * \rho_f \quad \text{(Eq.1)}$$

$$\rho(t) = \frac{\left(1+\frac{h_f-h_0}{h_0}\right)*\left(1+\frac{D_f-D_0}{D_0}\right)^2}{\left(1+\frac{1}{\alpha}*\frac{D(t)-D_0}{D_0}\right)*\left(1+\frac{D(t)-D_0}{D}\right)^2} * \rho_f \quad \text{(Eq. 2)}$$

$$\alpha = \frac{D_f-D_0}{D_0} * \frac{h_0}{h_f-h_0} \quad \text{(Eq. 3)}$$

where $\rho(t)$ is the instantaneous density of the sample, ρ_f the final density, h_f the final height, h_0 the initial height, $h(t)$ the instantaneous height, D_f the final diameter, D_0 the initial diameter and $D(t)$ the instantaneous diameter.

The thermal cycle was controlled by a specific homemade Labview software. It used a PID controller based on the temperature measured by pyrometers. The incident power delivered by the generator was continuously adjusted during the sintering cycle to match the measured temperature with the set temperature. At temperatures below 250°C (minimal temperature

detected by the pyrometer), the MW incident power was manually sent until the pyrometer detects a temperature of 250°C. It also recorded the data (power, temperature, images) useful to control the thermal treatment and to plot the dilatometric curves.

2.3. The sintering cell

The green samples were positioned in a sintering cell, used as an insulating box (Figure 1a and 1b) in order to optimize samples' insulation and guarantee their homogeneous heating. This sintering cell has been designed and tested during previous studies [33]. It was mainly made of different plates of aluminosilicate fibers (*KVS 184–400, RATH®*), used as thermal insulator. This material was used because it meets the requirements of MW applications: transparency to MW, stability at high temperature (to 1800 °C) and low thermal conductivity (0.33 $W.m^{-1}.K^{-1}$ at 1400 °C). Inside the cell, the sample was placed on two alumina sample holders to record images of its flat surface. A SiC ring was used as susceptor to initiate samples' heating. A low-loss mullite tube (*C610, AMTS*) surrounded the sample. This tube was used to minimize the susceptor radiation to the sample at high temperature.

2.4. Heating of pellets in a single-mode MW cavity

For a better understanding of MW/material interactions, direct heating of the samples in a SAIREM single-mode MW cavity was carried out. Small pieces (dimensions: 5*5*5 mm) cut from the three components of the sintering cell were also heated. The single-mode setup used in this study was well described by Ghorbel *et al.* [36]. Briefly, the cavity was composed of a 2.45 GHz MW generator (*Sairem GMSP10, Solid State30*), a WR340 waveguide, an iris, apertures with cylindrical chimneys (to measure temperature with a pyrometer) and a short-circuit piston. Before heating experiments, it was necessary to determine the conditions to obtain resonance in the cavity (superposition of incident and reflected waves). Therefore,

firstly, the samples were placed at a fixed position (in front of the chimney) in the cavity and the cavity length was slightly adjusted by the short-circuit piston. This was made with a Vector Network Analyzer (*Rohde & Schwarz*). The reflected power was monitored and reached a minimum value in the resonance conditions. For this study, all the pellets (diameter of 12 mm) were placed in the cavity without susceptor and thermal insulator, to obtain a configuration of direct MW heating. The pellets were heated with a constant forwarded power of 100 W applied during 9 min. The temperature at the surface of the pellet was measured by an IR pyrometer (*Fluke® Process Instruments, 27 E3ML-F1-V-0-0*) operating at a wavelength of 2.4 µm and an emissivity of 0.5.

2.5. Characterization of sintered samples

Densities of sintered samples were measured by Archimedes' method according to the standard ISO18754 [35]. The theoretical densities of alumina and 3Y-TZP were used to calculate the relative densities: 3.99 $g.cm^{-3}$ and 6.07 $g.cm^{-3}$.

Image analysis was carried out in a ZEISS SUPRA 55VP Scanning Electron Microscopy. Before observation, the samples were cut, polished until mirror surface finishing and thermally etched at 1480 °C during 10 min. Thermal etching was carried out in a tubular furnace, previously heated at 1480°C. The sample was then quickly inserted in the hot zone of the furnace. The average grain sizes of alumina and zirconia phases were measured by image analysis using the ImageJ software on at least 400 grains, at different locations of the cut surfaces (near the edge and at the center).

3. Results and discussions

3.1. Densification of the samples

The sintered relative densities of each sample are given in Table 1. All sintered samples are almost fully dense (relative density higher than 96 % T.D.). No significant difference between the various samples and the two configurations of MW sintering can be highlighted.

Table 1: Relative densities of the sintered samples

Pellets	Type of sintering	Sintered relative density (%)
A	CV	97.7
	MW-SiC	98.3
	MW-noSiC	97.5
A-10Z	CV	97.3
	MW-SiC	97.1
	MW-noSiC	97.5
A-20Z	CV	96.5
	MW-SiC	97.7
	MW-noSiC	97.0
3YZ	CV	96.3
	MW-SiC	98.6
	MW-noSiC	97.6

Figure 2a, 2c and 2e show densification vs temperature curves for each material during CV, MW-SiC and MW-noSiC sintering configurations. The corresponding derivative curves are given in Figure 2b, 2d and 2f.

For the two composites and for three configurations (CV, MW-SiC and MW-noSiC), the densification starts at higher temperatures, in comparison with alumina. It is known that zirconia has a delaying effect on densification of ZTA, compared to densification of monolithic alumina. This delaying effect has already been noted in CV and MW sintering [34, 37]. Different authors calculated a higher activation energy for sintering of ZTA composites than for alumina or zirconia [38, 39].

Some differences are noted when comparing the curves of each material between the three configurations. The densification curves for the MW-SiC configuration are shifted towards lower temperatures, in comparison with the curves for the CV configuration, especially in the intermediate stage of sintering. To try to quantify these differences, Table 2 indicates the temperatures at which a relative density of 75 % is reached for each configuration of sintering and each sample. The difference of these temperatures between the CV and MW-SiC configurations (T_{CV}-$T_{MW\text{-}SiC}$) is positive for the four samples. It means that MW sintering with a susceptor seems to favor densification at lower temperatures, compared with CV sintering. But it is difficult to explain the evolution of T_{CV}-$T_{MW\text{-}SiC}$ from A to 3YZ samples. The shifting of densification curves towards lower temperatures for MW sintering has already been observed by Zuo *et al.* for alumina [33, 40]. It has been attributed by these authors to a possible non-thermal microwave effect, which had already been proposed by Rybakov *et al.* [41]. But the different methods used to measure temperature (thermocouples for CV sintering and pyrometer for MW sintering) can also have an influence on these results. Even if the pyrometer was calibrated, the measurement of temperature by pyrometry is always affected by an uncertainty, linked to the dependency to emissivity.

The comparison between the curves of MW-SiC and MW-noSiC configurations reveals interesting difference of behaviour. The densification curves are shifted towards higher temperatures for the MW-noSiC configuration, especially for the initial and intermediate stages

of sintering. Table 2 presents the temperatures at which a relative density of 75% is reached for the MW-SiC and MW-noSiC configurations and the differences between these temperatures ($T_{MW\text{-}noSiC}$ -$T_{MW\text{-}SiC}$). Moreover, Table 3 presents the temperatures of onset of densification for the two configurations and the difference between these temperatures. These differences of temperature (Tables 2 and 3) are the lowest for the A-20Z and 3YZ samples, in comparison with the A sample. The same tendency is observed for the temperature of maximum densification rate in the derivative curves. Table 4 reports these temperatures for MW-SiC and MW-noSiC configurations and the differences between these temperatures. These temperatures are shifted towards higher temperatures in the absence of SiC. The shifting is lower for the A-20Z and 3YZ samples, in comparison with the A sample. In the absence of SiC, MW heating is more difficult but this difficulty decreases in the presence of 3Y-TZP. The case of A-20Z shows a positive effect of 3Y-TZP for the MW heating of the composite. As previously mentioned, the A-10Z sample does not follow this trend. The temperature was measured by a pyrometer for the MW-SiC and MW-noSiC configurations. The presence or absence of the SiC ring in the sintering cell changes the sample's surroundings and, thus, the radiations received by the pyrometer. It can be a source of error for temperature measurement and thus, for reliable comparison between data from MW-SiC and MW-noSiC configurations. This potential source of error was taken into account by calibrating the pyrometer's emissivity ratio for each material and both configurations.

Table 2: Temperatures at which a relative density of 75% is reached during CV, MW-SiC and MW-noSiC sintering and difference between these temperatures

Samples	T_{CV}	$T_{MW\text{-}SiC}$	$T_{MW\text{-}noSiC}$	$T_{CV} - T_{MW\text{-}SiC}$	$T_{MW\text{-}noSiC} - T_{MW\text{-}SiC}$
A	1430	1333	1393	97	60
A-10Z	1472	1421	1504	51	83
A-20Z	1538	1456	1498	82	42
3YZ	1383	1285	1323	98	38

Table 3: Temperature of onset of densification for MW-SiC and MW-noSiC configurations and difference between these temperatures

Samples	Temperature of onset of densification for MW-SiC	Temperature of onset of densification for MW-noSiC	Difference of temperature ($T_{MW\text{-}noSiC} - T_{MW\text{-}SiC}$)
A	990	1105	115
A-10Z	984	1193	209
A-20Z	1133	1188	55
3YZ	945	1001	55

Table 4: Temperature of maximum densification rate for MW-SiC and MW-noSiC configurations and difference between these temperatures

Samples	Temperature of maximum densification rate for MW-SiC	Temperature of maximum densification rate for MW-noSiC	Difference of temperature ($T_{MW-noSiC}$-T_{MW-SiC})
A	1302	1367	65
A-10Z	1378	1484	106
A-20Z	1421	1464	43
3YZ	1310	1311	1

3.2. Microstructure of sintered samples

Figure 3 shows the SEM images of the four samples sintered with the MW-SiC configuration. For each sample, an image at the center (Figure 3**Erreur ! Source du renvoi introuvable.**a, 3 c, 3e and 3g) and an image at the edge (Figure 3b, 3d, 3f and 3h) of the polished surfaces are shown. The 3YZ samples present a very fine and homogeneous microstructure, in comparison with the A sample. In the case of composites, the zirconia grains are located at the alumina grain boundaries. Few zirconia aggregates are also visible. A refinement of the alumina grains is also noted in the presence of zirconia in the composites, in comparison with the A sample.

Figure 4 shows the average grain sizes and the standard deviations measured on the images for each sample and each sintering configuration. In the three cases, the alumina average grain size decreases with the increase of zirconia volume fraction. The inhibition of alumina grain growth in the presence of zirconia grains as a second phase is well-known in the literature for CV sintering [37, 42, 43] and MW sintering [34, 44]. For the two composites, comparison between the average grain sizes at the edge and at the center of the samples shows close values, which

indicates that a quite homogeneous heating took place inside the samples. No significant difference in average grain sizes and standard deviations can be highlighted between CV, MW-SiC and MW-noSiC sintering. For the two monolithic samples, more significant differences are observed between the edge and the center. The average grain sizes of the A sample are higher at the centre, compared with the surface for CV and MW-SiC configuration (Figure 4a and 4b). This is not the case for MW-noSiC configuration, for which the average grain size of alumina is higher at the surface (Figure 4c). The standard deviation is around 1 μm for the three sintering configurations for alumina. For the 3YZ samples, the average grain sizes are slightly higher at the surface. The standard deviations of the grain size distribution for 3YZ are around 0.2–0.4 μm.

3.3.Evolution of MW powers during sintering

Figure 5 presents the evolution of measured temperature vs time (a, c, e, g) and incident and absorbed MW powers vs temperature (b, d, f, h) during the thermal cycles for the four samples. The curves of measured temperature vs time show that the set heating step was quite correctly followed during the thermal cycles by to the PID regulation. Small disturbance zones in the range 1400-1500°C in the heating step are visible for A and A-20Z for the MW-SiC sintering cycles. When sintering without the SiC ring, a delay in the beginning of heating is observed, in comparison with sintering with SiC. This delay is 15, 25, 13 and 10 minutes for A, A-10Z, A-20Z and 3YZ, respectively. For A, A-20Z and 3YZ, this delay decreases when the volume fraction of zirconia increases. It is the sign of an easiest heating capability of the samples under MW. But surprisingly, the A-10Z sample does not follow this trend: it needs more time to initiate heating than A whereas A-10Z contains zirconia.

The incident and absorbed MW powers increase with temperature for all the samples sintered with SiC. It is known that in the presence of SiC, the MW heating is mainly hybrid, that is to

say: the pellets heat in the bulk by direct coupling with microwave and on the surface by radiation of the susceptors. In this case, the interaction between MW and SiC can have an important influence. In particular, a dramatic increase of incident power was necessary to heat the A sample from 1400 to 1500°C. An increase of absorbed power is also observed in this temperature range. It corresponds to the disturbance zone in the temperature vs time curve for this sample (Figure 5a). Such a disturbance zone is not visible for the three other samples. This difference of behaviour between the A and the zirconia-containing samples can be explained by the difference of MW coupling. The A sample weakly interacts with the MW due to the low dielectric properties of alumina, especially the low values of ε'', in comparison with the values for 3Y-TZP [24]. Heuguet *et al.* [29] calculated the electric field distribution in the case of MW heating of alumina sintered with a SiC or a 3Y-TZP susceptor. In the case of 3Y-TZP susceptor, the calculated electric field within the alumina sample was significantly higher than the one calculated within the sample heated with the SiC susceptor. Moreover, they also obtained lower values of electric field inside the alumina sample when the electrical conductivity of SiC was increased (the SiC electrical conductivity is known to highly increase with temperature [45] and penetration depth of MW is inversely proportional to electrical conductivity [20]). They concluded that the SiC susceptor favored a mainly indirect heating of alumina whereas the 3Y-TZP one mostly led to a volumetric heating. These results can help to understand the difference of MW powers between the different samples. The screening effect of SiC at high temperature and the low MW coupling of alumina can explain the difficulty to heat the A sample from 1400°C, and so, the high values of MW incident powers. The presence of zirconia in the A-10Z, A-20Z and 3YZ samples can explain their better coupling with MW, which favors a more direct MW/sample interaction and so, lower values of MW incident powers.

For the samples sintered without SiC, the evolution of power vs temperature is different. The incident power is quite constant from 400 to 1200°C for the A sample and slightly decreases

for the three other samples in the same temperature range. From 1200 to 1550°C, it increases for the four samples. The absorbed power is quite constant until 1200°C and increases for the higher temperatures.

In addition to these curves, Supplementary Figure 1 presents the evolution of incident and absorbed powers vs temperature for the A-10Z composite sintered twice with both sintering cells (Supplementary Figure 1a for MW-SiC and Supplementary Figure 1b for MW-noSiC). For each configuration, the incident and absorbed powers vary similarly during the two sintering cycles. It proves that the thermal treatments were reproducible for a given material and a given sintering cell.

3.4. Heating of green pellets in a single-mode MW cavity

Figure 6 shows the evolution of temperature for the four samples submitted to a constant incident power in a MW single-mode cavity. Different behaviours can be highlighted. The 3YZ sample started to heat with an initial heating rate of around 198°C/min. A temperature of 300°C was achieved after 78 s. Then, a thermal runaway was observed and the MW power was turned off to avoid damaging the cavity. For the A sample, the onset of heating takes place after 23 seconds and then, temperature increases and quickly reaches a plateau at 170°C. The two composites exhibit an intermediate behaviour between the two monolithic materials. The onset of heating happens after 23 s for A-10Z and after 12 s for A-20Z. Then, A-10Z reaches a plateau at 238°C whereas A-20Z continues to heat with a low heating rate and reaches 298°C after 9 minutes.

3.5. Discussions about MW/materials interaction

It is known that alumina and 3Y-TZP exhibit different dielectric properties, and thus different MW coupling capability. Therefore, an intermediate behaviour is expected for ZTA

composites. In particular, addition of zirconia in alumina matrix is expected to increase the coupling with MW and, thus to facilitate MW heating. This evolution of behaviour from monolithic alumina to monolithic zirconia is visible in the heating experiments carried out in the single-mode cavity. The evolution of temperature vs time in single-mode cavity (Figure 6) can be considered as a correct "image" of the dielectric properties of the material. It has to be noted that the duration of heating was limited to 9 minutes here to avoid damaging the cavity, whose walls could not be cooled. Evolution of MW powers during the sintering cycles in the multimode cavity (Figure 5) showed the influence of the materials to heat, especially in the case of sintering without SiC. Similarly, the densification curves evidenced different behaviours between the samples. As previously mentioned, comparison between CV and MW sintering is quite difficult because of the different methods used to measure temperatures. But comparison between MW-SiC and MW-noSiC show some interesting results. As previously explained, the comparison between these two configurations is more reliable because temperatures were measured by the pyrometer in the two cases and the pyrometer was calibrated for both configurations. As previously noted, the presence or absence of SiC in the sintering cell changes the environment of the sample, *i.e.*, the sample receives radiation by SiC when it is present. Heating the samples without SiC is less and less difficult when increasing the volume fraction of zirconia. But the ZTA samples with 10 vol% 3Y-TZP did not behave like the one with 20 vol% 3Y-TZP. This difference can be explained by the percolation threshold of 16 vol% for the zirconia second phase in the ZTA composites [42, 46]. Below this threshold, the zirconia grains or few zirconia grain aggregates are isolated in the alumina matrix. When the temperature increases, they heat preferentially due to the increase of ε'' of 3Y-TZP. Then, each isolated zirconia grain or aggregate can heat few surrounding alumina grains by conduction. On the contrary, above the percolation threshold, the zirconia grains form a path in the alumina matrix. Thus, it can be hypothesized that almost all the alumina grains can be heated by conduction by

the zirconia grains. This possible mechanism of heating can explain that it is necessary to add more than 16 vol% of zirconia in ZTA to obtain a visible effect on MW heating. Testing other ZTA samples with different volume fractions of zirconia (below 10%, above 20% and intermediate value between 10 and 20%) could help to confirm this hypothesis.

Few differences were obtained in the final properties of the MW-SiC and MW-noSiC sintered samples. The densification curves show small differences between MW-SiC and MW-noSiC in the final stage of sintering. All samples reached almost full densification. With regard to MW-SiC sintering, the SiC ring mostly couples with MW, resulting in a mainly indirect radiative heating, which is comparable to a CV sintering. For the microstructures, some differences in the homogeneity were observed between the A samples and the zirconia-containing ones. The differences between the average grain sizes at the center and the edge and the standard deviations are higher for the A samples than for the three zirconia-containing samples, especially in the case of the MW-noSiC configuration (in comparison with the MW-SiC configuration). Therefore the microstructure of the A sample was more affected by the change of sintering cell than the three other samples. It confirms what was previously said: a large part of the electromagnetic field is probably absorbed by SiC which then heats alumina by radiation. In the case of the two composites and 3YZ, zirconia favours a more direct MW/material interaction. Concerning the two composites, the presence of zirconia in an alumina matrix seems to play a role of an "internal susceptor", especially for a volume fraction of zirconia higher than the percolation threshold.

Despite these small differences in the final microstructures, it has to be noted that all the samples were fully densified with and without SiC, especially low-loss alumina. It can be explained by the influence of the materials constituting the sintering cell (*i.e.*, mullite and insulator). In a previous study [30], the authors studied the influence of the same sintering cell on the sintering of alumina and 3Y-TZP in the multimode cavity. They found that sintering of

alumina was possible with the sintering cell without the SiC ring. Figure 7 shows the evolution of temperature vs time for small pieces cut from the components of the sintering cell, heated in the single-mode cavity. This graph confirms that mullite and aluminosilicate insulators can heat under MW, even if they couple less than SiC. It confirms the results obtained by Garnault *et al.* [28] who showed that an insulating material can absorb a part of the MW energy in the case of MW sintering of alumina in a single-mode cavity. Therefore, in the case of MW sintering in a multimode cavity (where the weight of insulating material is higher than in a single-mode cavity), the absence of the SiC ring did not lead to a real direct MW sintering. All the components of the sintering cell can play the role of susceptor and help to heat the sample. It is especially the case for low-loss materials such as alumina. Consequently, the sintering cell can partially hide the possible effect of the material to heat and explain why all the sintered samples have close characteristics.

The sintering experiments performed in this study in a multimode cavity could be completed by deeper investigations in a single-mode cavity. This resonant cavity enables to maximize the MW/material interaction by optimizing the sample position and obtaining the resonance conditions. Simulations of the propagation of the electromagnetic field with different materials could also be interesting to complete the experimental work.

4. Conclusion

In this study, four different samples (alumina, 3Y-TZP and two ZTA composites) were sintered in a MW multimode cavity with two different sintering cells (with and without SiC) in order to investigate the effect of samples' composition on densification and microstructure of sintered specimens. The characterizations performed on the sintered samples show very similar results: all the sintered samples are fully dense and have a fine microstructure.

The evolution of MW powers during the thermal cycles and the densification curves highlight some differences of behaviour related to the material to heat. The presence of zirconia facilitates the heating in the composites, in comparison with monolithic alumina.

Experiments performed in a single-mode cavity evidence more important difference of behaviour between the different samples. In particular, the high coupling capability of 3Y-TZP was translated by its rapid heating and a thermal runaway. An intermediate behaviour between alumina and zirconia was noted for the two composites (no thermal runaway and higher temperatures achieved than for alumina alone). These experiments show the interest of sintering ZTA composites in a single-mode cavity to investigate deeper the MW/material interactions.

Acknowledgements

The authors gratefully acknowledge the support of Marilyne Mondon for scanning electron microscopy and Gilles Blanc for metallographic preparation.

References

[1] H. Reveron, J. Chevalier, Yttria-stabilized zirconia as a biomaterial: from orthopedic towards dental applications, Encyclopedia of Materials: Technical Ceramics and Glasses, 3 (2021) 540-552. https://doi.org/10.1016/B978-0-12-818542-1.00030-8

[2] P. Shelar, H. Abdolvand, S. Butler, On the behaviour of zirconia-based dental materials: A review, J. Mech. Behav. Biomed. Mater. 124 (2021) 104861. https://doi.org/10.1016/j.jmbbm.2021.104861

[3] F.A. Al-Sanabani, A. Madfa, N.H. Al-Qudaimi, Alumina ceramic for dental applications: A review article, Am. J. Mater. Res. 1 (2014) 26-34

[4] D. Duraccio, F. Mussano, M.G. Faga, Biomaterials for dental implants: current and future trends, J. Mater. Sci. 50 (2015) 4779-4812. https://doi.org/10.1007/s10853-015-9056-3

[5] E.H. Kisi, C.J. Howard, Crystal structures of zirconia phases and their inter-relation, Key Eng. Mater. 153-154 (1998) 1-36. https://doi.org/10.4028/www.scientific.net/KEM.153-154.1

[6] P. Li, I.W Chen, J.E. Penner-Hahn, Effects of dopant on zirconia stabilization - An X-ray absorption study: III Charge-compensating dopants, J. Am. Ceram. Soc. 75 (1994) 1289-1295. https://doi.org/10.1111/j.1151-2916.1994.tb05404.x

[7] J. Chevalier, L. Gremillard, A.V. Virkar, D.R. Clarke, The tetragonal-monoclinic transformation in zirconia: lessons learned and future trends, J. Am. Ceram. Soc. 92 (2009) 1901-1920. https://doi.org/10.1111/j.1551-2916.2009.03278.x

[8] J. Chevalier, B. Cales, J.M. Drouin, Low-temperature aging of Y-TZP ceramics, J. Am. Ceram. Soc. 82 (1999) 2150-2154. https://doi.org/10.1111/j.1151-2916.1999.tb02055.x

[9] M. Orlovska, L. Húlek, L. Baca, V. Kovar, K. Tomanova, M. Kitzmantel, M. Janek, E. Neubauer, Study of the alumina sintering process with a low zirconia content, Ceram. Inter. 48 (2022) 2736-2743. https://doi.org/10.1016/j.ceramint.2021.10.060

[10] A.C.O. Lopes, P.G. Coelho, L. Witek, E.B. Benalcázar Jalkh, L.A. Gênova, K.N. Monteirof, P.F. Cesar, P.N. Lisboa-Filho, E.T.P Bergamo, I.S. Ramalho, T.M.B. Campos, E.A. Bonfante, Microstructural, mechanical, and optical characterization of an experimental aging-resistant zirconia-toughened alumina (ZTA) composite, Dent. Mater. 36 (2020) 365-374. https://doi.org/10.1016/j.dental.2020.08.010

[11] O. Yu Zadorozhnaya, T.A. Khabas, O.V. Tiunova, S.E. Malykhin, Effect of grain size and amount of zirconia on the physical and mechanical properties and the wear resistance of

zirconia-toughened alumina, Ceram. Inter. 46 (2020) 9263-9270. https://doi.org/10.1016/j.ceramint.2019.12.180

[12] Y. Lakhdar, C. Tuck, J. Binner, A. Terry, R. Goodridge, Additive manufacturing of advanced ceramic materials, Progr. Mater. Sci. 116 (2021) 100736. https://doi.org/10.1016/j.pmatsci.2020.100736

[13] S.M. Olhero, P.M.C. Torres, J. Mesquita-Guimaraes, J. Baltazar, J. Pinho-da-Cruz, S. Gouvei, Conventional *versus* additive manufacturing in the structural performance of dense alumina-zirconia ceramics: 20 years of research, challenges and future perspectives, J. Manufact. Process. 77 (2022) 838-879. https://doi.org/10.1016/j.jmapro.2022.02.041

[14] M. Renaux, D. Méresse, J. Pellé, A. Thuault, C. Morin, C. Nivot, C. Courtois, Mechanical modelling of microwave sintering and experimental validation on an alumina powder, J. Eur. Ceram. Soc. 41 (2021) 6617-6625. https://doi.org/10.1016/j.jeurceramsoc.2021.06.013

[15] V. Nečina, W. Pabst, Influence of the heating rate on grain size of alumina ceramics prepared via spark plasma sintering (SPS), J. Eur. Ceram. Soc. 40 (2020) 3656-3662. https://doi.org/10.1016/j.jeurceramsoc.2020.03.057

[16] B. Suleiman, H. Zhang, Y. Ding, Y. Li, Microstructure and mechanical properties of cold sintered porous alumina ceramics, Ceram. Inter. 48 (2022) 13531-13540. https://doi.org/10.1016/j.ceramint.2022.01.232

[17] J. Brie, T. Chartier, C. Chaput, C. Delage, B. Pradeau, F. Caire, M.-P. Boncoeur, J.-J. Moreau, A new custom made bioceramic implant for the repair of large and complex craniofacial bone defects, J. Cranio-Maxillo-Facial Surg. 41 (2013) 403-407. http://dx.doi.org/10.1016/j.jcms.2012.11.005

[18] C. Singh, V. Khanna, S. Singh, Sustainability of microwave heating in materials processing technologies, Mater. Today Proceed. 73 (2023) 241-248. https://doi.org/10.1016/j.matpr.2022.07.216

[19] M. Oghbaei, O. Mirzaee, Microwave versus conventional sintering: A review of fundamentals, advantages and applications, J. Alloys Compd. 494 (2010) 175-189. https://doi.org/10.1016/j.jallcom.2010.01.068

[20] R.R. Mishra, A.K. Sharma, Microwave-material interaction phenomena: Heating mechanisms, challenges and opportunities in material processing, Compos. Part Appl. Sci. Manuf. 81 (2016) 78-97. https://doi.org/10.1016/j.compositesa.2015.10.035

[21] R. Benavente, M.D. Salvador, F.L. Penaranda-Foix, E. Pallone, A. Borrell, Mechanical properties and microstructural evolution of alumina–zirconia nanocomposites by microwave sintering, Ceram. Int. 40 (2014) 11291-11297. https://doi.org/10.1016/j.ceramint.2014.03.153

[22] R.R. Menezes, R.H.G.A. Kiminami, Microwave sintering of alumina–zirconia nanocomposites, J. Mater. Process. Technol. 203 (2008) 513-517. https://doi.org/10.1016/j.jmatprotec.2007.10.057

[23] R. Vasudevan, T. Karthik, S. Ganesan, R. Jayavel, Effect of microwave sintering on the structural and densification behavior of sol-gel derived zirconia toughened alumina (ZTA) nanocomposites, Ceram. Int. 39 (2013) 3195-3204. https://doi.org/10.1016/j.ceramint.2012.10.004

[24] M. Arai, J.G.P. Binner, T.E. Cross, Comparison of techniques for measuring high-temperature microwave complex permittivity: Measurements on an alumina/zircona system, J. Microw. Power Electromagn. Energy. 31 (1996) 12-18. https://doi.org/10.1080/08327823.1996.11688287

[25] M. Bhattacharya, T. Basak, A review on the susceptor assisted microwave processing of materials, Energy. 97 (2016) 306-338. https://doi.org/10.1016/j.energy.2015.11.034

[26] H. Curto, A. Thuault, F. Jean, M. Violier, V. Dupont, J.-C. Hornez, A. Leriche, Coupling additive manufacturing and microwave sintering: A fast processing route of alumina ceramics, J. Eur. Ceram. Soc. 40 (2020) 2548-2554. https://doi.org/10.1016/j.jeurceramsoc.2019.11.009

[27] C. Manière, T. Zahrah, E.A. Olevsky, Fully coupled electromagnetic-thermal-mechanical comparative simulation of direct vs hybrid microwave sintering of 3Y-ZrO_2, J. Am. Ceram. Soc. 100 (2017) 2439-2450. https://doi.org/10.1111/jace.14762

[28] T. Garnault, D. Bouvard, J.-M. Chaix, S. Marinel, C. Harnois, Is direct microwave heating well suited for sintering ceramics?, Ceram. Int. 47 (2021) 16716-16729. https://doi.org/10.1016/j.ceramint.2021.02.242

[29] R. Heuguet, S. Marinel, A. Thuault, A. Badev, Effects of the susceptor dielectric properties on the microwave sintering of alumina, J. Am. Ceram. Soc. 96 (2013) 3728-3736. https://doi.org/10.1111/jace.12623

[30] N. Khalile, C. Petit, C. Meunier, F. Valdivieso, Hybrid microwave sintering of alumina and 3 mol% Y_2O_3-stabilized zirconia in a multimode cavity – Influence of the sintering cell, Ceram. Inter. 48 (2022) 18143-18150. https://doi.org/10.1016/j.ceramint.2022.03.072

[31] N. Khalile, C. Meunier, C. Petit, F. Valdivieso, B. Coppola, P. Palmero, Microwave sintering of dense and lattice 3Y-TZP samples shaped by digital light processing, Ceram. Int. 49 (2023) 7350-7358. https://doi.org/10.1016/j.ceramint.2022.10.194

[32] D. Żymełka, S. Saunier, D. Goeuriot, J. Molimard, Densification and thermal gradient evolution of alumina during microwave sintering at 2.45GHz, Ceram. Int. 39 (2013) 3269-3277. https://doi.org/10.1016/j.ceramint.2012.10.015

[33] F. Zuo, C. Carry, S. Saunier, S. Marinel, D. Goeuriot, Comparison of the microwave and conventional sintering of alumina: effect of MgO doping and particle size, J. Am. Ceram. Soc. 96 (2016) 1732-1737. https://doi.org/10.1111/jace.12320

[34] C. Meunier, F. Zuo, N. Peillon, S. Saunier, S. Marinel, D. Goeuriot, In situ study on microwave sintering of ZTA ceramic: Effect of ZrO_2 content on densification, hardness, and toughness, J. Am. Ceram. Soc. 100 (2017) 929-936. https://doi.org/10.1111/jace.14658

[35] International Organisation for Standardization, in: Fine Ceramics (Advanced Ceramics, Advanced Technical Ceramics) - Determination of Density and Apparent Porosity, ISO18754, 2020, 10 p.

[36] I. Ghorbel, P. Ganster, N. Moulin, J. Bruchon, Experimental and numerical thermal analysis for direct microwave heating of silicon carbide, J. Am. Ceram. Soc 104 (2021) 302-312. https://doi.org/10.1111/jace.17451

[37] F.F. Lange, T. Yamaguchi, B.I. Davis, P.E. d. Morgan, Effect of ZrO_2 inclusions on the sinterability of Al_2O_3, J. Am. Ceram. Soc. 71 (1988) 446-448. https://doi.org/10.1111/j.1151-2916.1988.tb05892.x

[38] J. Wang, R. Raj, Activation energy for the sintering of two-phase alumina/zirconia ceramics, J. Am. Ceram. Soc. 74 (1991) 1959-1963. https://doi.org/10.1111/j.1151-2916.1991.tb07815.x

[39] H.L.C. Pulgarín, M.P. Albano, Sintering and microstrusture of Al_2O_3 and Al_2O_3-ZrO_2 Ceramics, Proc. Mater. Sci. 8 (2015) 180-189. https://doi.org/10.1016/j.mspro.2015.04.062

[40] F. Zuo, A. Badev, S. Saunier, D. Goeuriot, R. Heuguet, S. Marinel, Microwave versus conventional sintering: Estimate of the apparent activation energy for densification of α-alumina and zinc oxide, J. Eur. Ceram. Soc. 34 (2014) 3103-3110. https://doi.org/10.1016/j.jeurceramsoc.2014.04.006

[41] K.I. Rybakov, V.E. Semenov, Mass transport in ionic crystals induced by the ponderomotive action of a high-frequency electric field, Phys. Rev. B. 52 (1995) 3030-3033. https://doi.org/10.1103/PhysRevB.52.3030

[42] K. Biotteau-Deheuvels, L. Zych, L. Gremillard, J. Chevalier, Effects of Ca-, Mg- and Si-doping on microstructures of alumina-zirconia composites, J. Eur. Ceram. Soc. 32 (2012) 2711-2721. https://doi.org/10.1016/j.jeurceramsoc.2011.11.011

[43] D. Casellas, M.M. Nagl, L. Llanes, M. Anglada, Microstructural coarsening of zirconia-toughened alumina composites, J. Am. Ceram. Soc. 88 (2005) 1958-1963. https://doi.org/10.1111/j.1551-2916.2005.00374.x

[44] M.W. Khalid, Y.I. Kim, M.A. Haq, D. Lee, B.S. Kim, B. Lee, Microwave hybrid sintering of Al_2O_3 and Al_2O_3-ZrO_2 composites, and effects of ZrO_2 crystal structure on mechanical properties, thermal properties, and sintering kinetics, Ceram. Int. 46 (2020) 9002-9010. https://doi.org/10.1016/j.ceramint.2019.12.147

[45] A. Kassiba, M. Tabellout, S. Charpentier, N. Herlin, J.R. Emery, Conduction and dielectric behaviour of SiC nano-sized materials, Solid State Comm. 115 (2000) 389-393. https://doi.org/10.1016/S0038-1098(00)00195-2

[46] C. Pecharromán, J. f. Bartolomé, J. Requena, J. s. Moya, S. Deville, J. Chevalier, G. Fantozzi, R. Torrecillas, Percolative Mechanism of aging in zirconia-containing ceramics for medical applications, Adv. Mater. 15 (2003) 507-511. https://doi.org/10.1002/adma.200390117.

Figures' captions

Figure 1: Scheme of the insulating box for MW sintering, front view (a) and inside top view (b)

Figure 2: Densification curves of the samples for CV (a), MW-SiC (b) and MW-noSiC (c) sintering

Figure 3: SEM micrographs and related grain size distributions of A (a, b), A-10Z (c, d), A-20Z (e, f) and 3YZ (g, h) in the centre (a, c, e, g) and in the surface (b, d, f, h) of the sintered samples (MW-SiC configuration)

Figure 4: Alumina and zirconia average grain sizes at the center and at the edges of the samples as a function of zirconia volume fraction for CV (a), MW-SiC (b) and MW-noSiC sintering (c)

Figure 5: Evolution of temperature vs time (a, c, e, g) and MW powers vs temperature (b, d, f, h) for the different thermal cycles: A (a, b), A-10Z (c, d), A-20Z (e, f), 3YZ (g, h) samples

Figure 6: Evolution of temperature vs time for the four samples heated in a MW single-mode cavity

Figure 7: Evolution of temperature vs time for small pieces of the components of the sintering cell (mullite, aluminosilicate insulator and SiC) heated in a MW single-mode cavity

Supplementary Figure 1: MW powers vs temperature for two identical thermal cycles carried out for the A-10Z samples for MW-SiC sintering (a) and MW-noSiC sintering (b)

Figure 1:

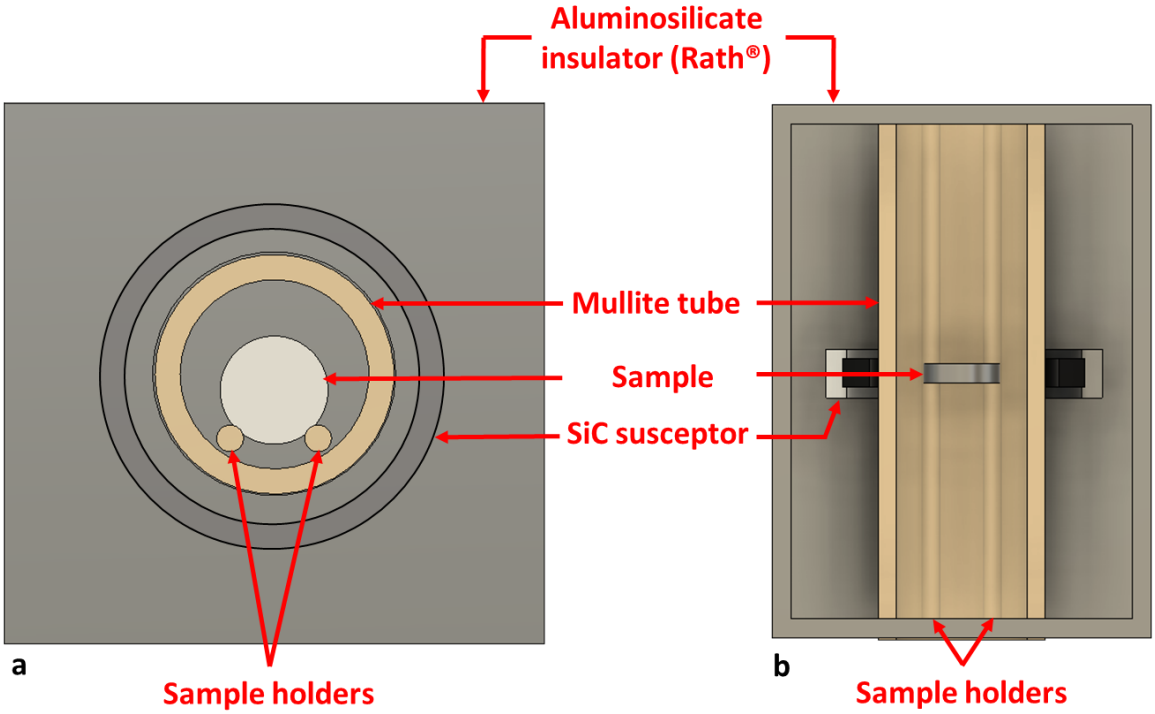
Aluminosilicate
insulator (Rath®)
Mullite tube
Sample
SiC susceptor
a
Sample holders
b
Sample holders

Figure 2:

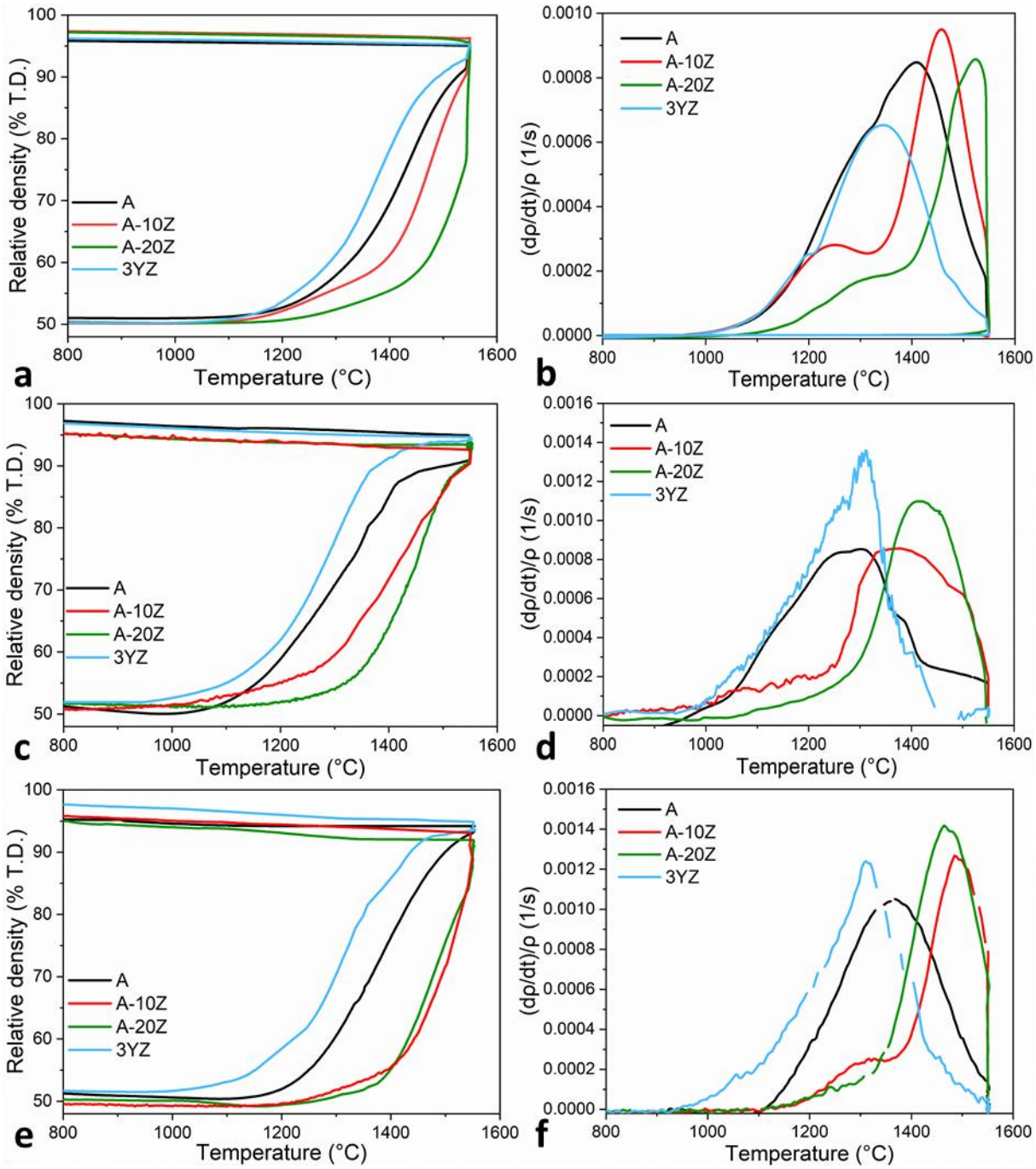
a
b
c
d
e
f
Relative density (% T.D.)
(dρ/dt)/ρ (1/s)
Temperature (°C)
A
A-10Z
A-20Z
3YZ

Figure 3:

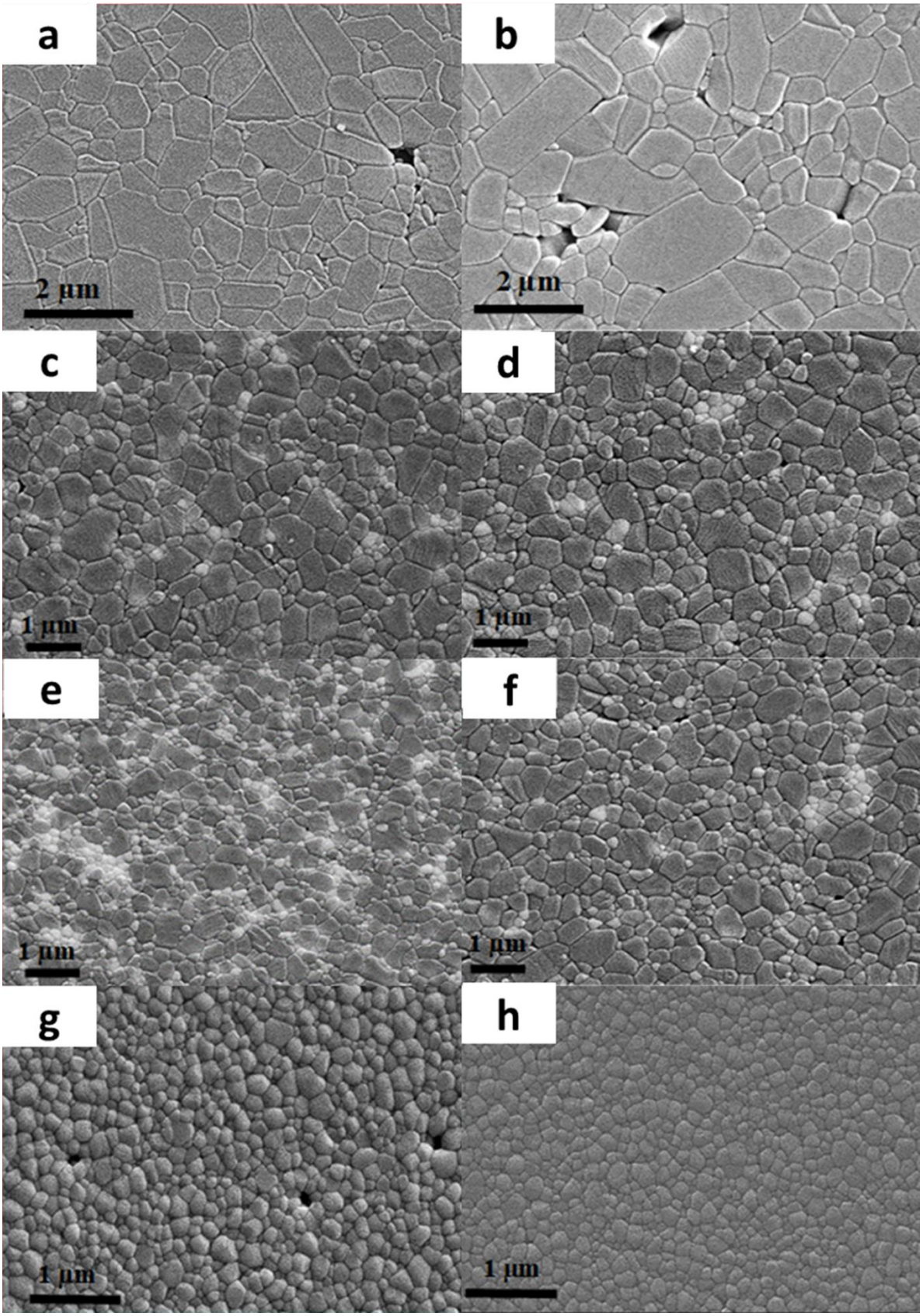

Figure 4:

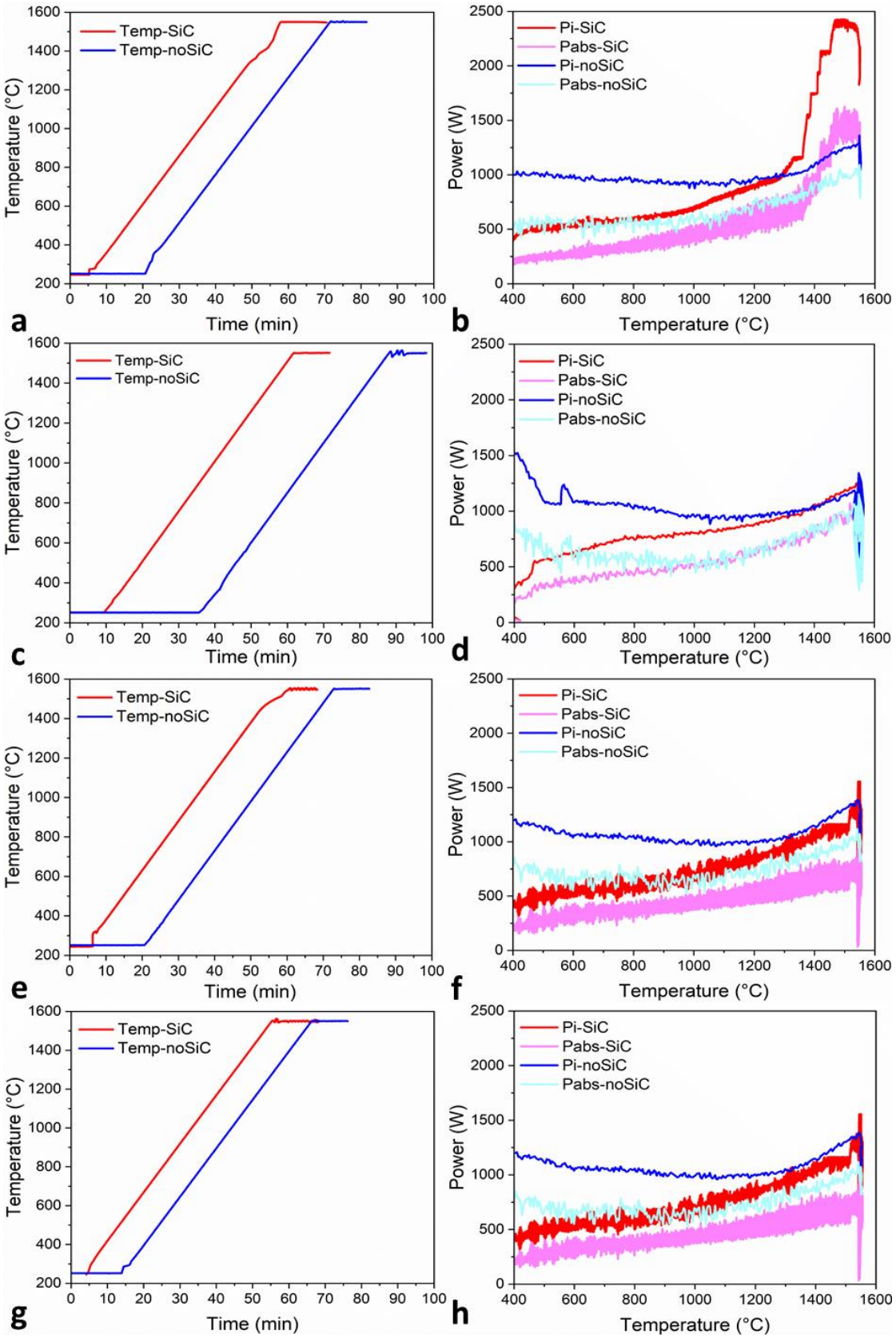
Temp-SiC
Temp-noSiC
Temperature (°C)
Time (min)
a
Pi-SiC
Pabs-SiC
Pi-noSiC
Pabs-noSiC
Power (W)
Temperature (°C)
b
c
d
e
f
g
h

Figure 5:

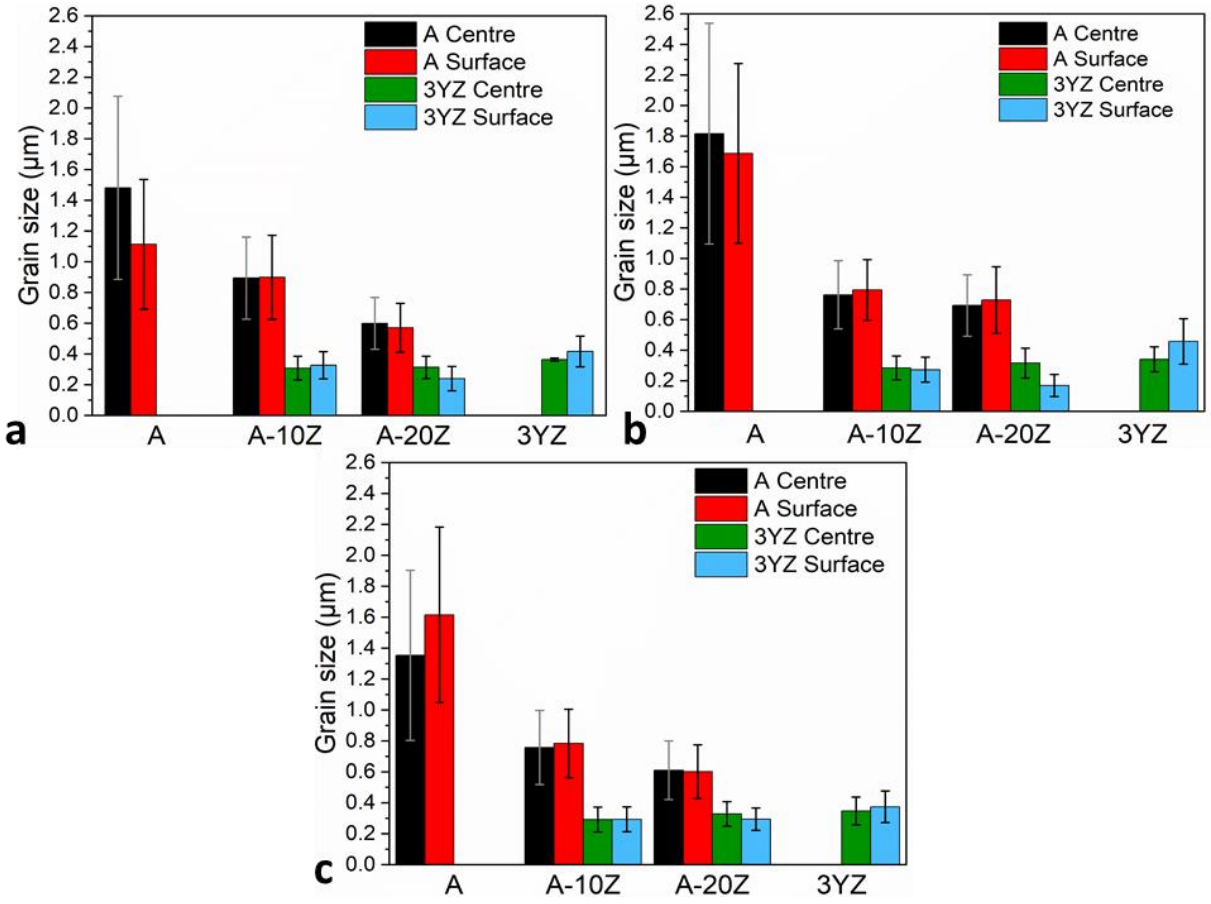
a
b
c
Grain size (µm)
A Centre
A Surface
3YZ Centre
3YZ Surface
A
A-10Z
A-20Z
3YZ
0.0
0.2
0.4
0.6
0.8
1.0
1.2
1.4
1.6
1.8
2.0
2.2
2.4
2.6

Figure 6:

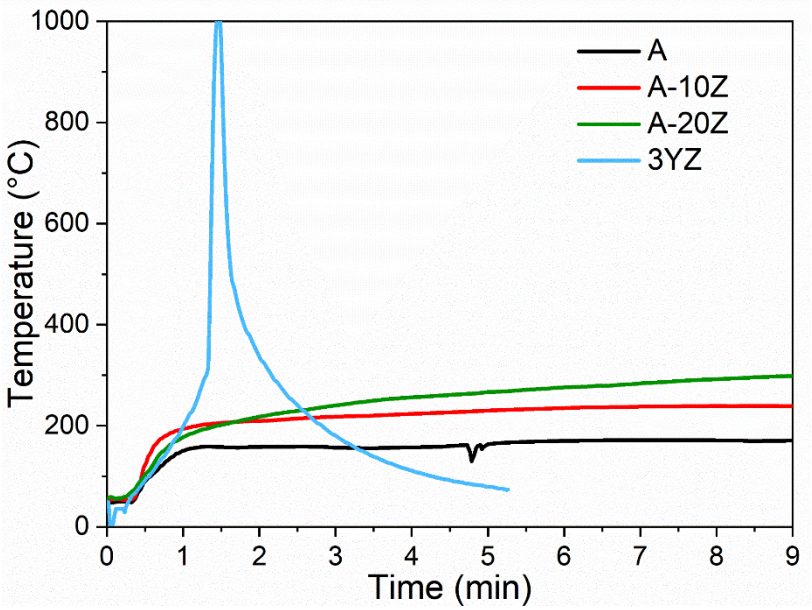
Temperature (°C)
Time (min)
A
A-10Z
A-20Z
3YZ
0
200
400
600
800
1000
0
1
2
3
4
5
6
7
8
9

Figure 7:

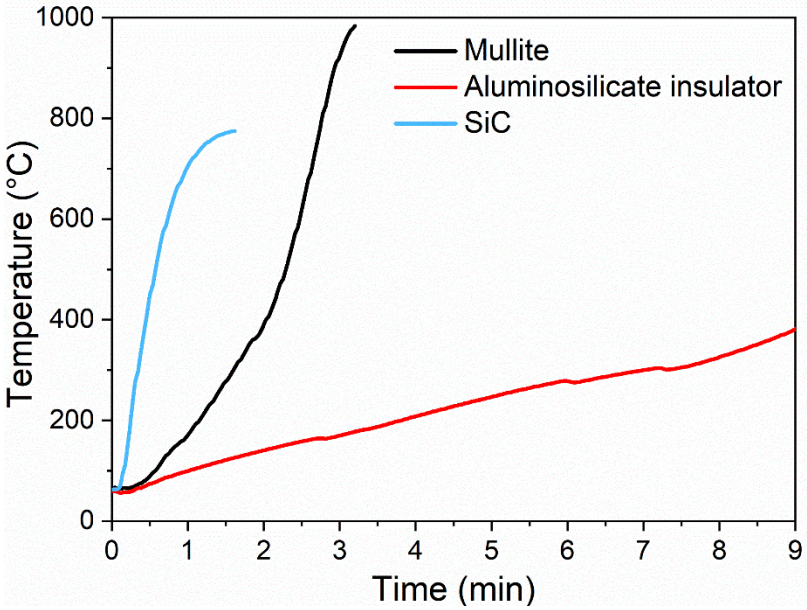
Mullite
Aluminosilicate insulator
SiC
Temperature (°C)
Time (min)
0
200
400
600
800
1000
0
1
2
3
4
5
6
7
8
9

Supplementary file: